4 Transverse Beam Emittance Measurement and Control

The beam emittance ϵ_{xyz} represents the volume of the beam occupied in the six dimensional phase space $(x, x', y, y', \phi, \delta)$, where x and y are the transverse positions, x' and y' are the transverse angles, ϕ is the time-like variable representing the relative phase of the beam, and δ is the relative beam momentum error. Using the notation of the beam matrix $\Sigma_{\rm beam}$ introduced in Chap. 1, the 6-dimensional emittance is

$$\epsilon_{xyz} = \det\, \Sigma_{\rm beam}^{xyz}\,. \tag{4.1}$$

Considering now only the horizontal plane, the corresponding 2-dimensional horizontal emittance is obtained from

$$\epsilon_x = \sqrt{\langle x^2\rangle\langle x'^2\rangle - \langle xx'\rangle^2}\,, \tag{4.2}$$

where the first moments have been subtracted, and the average ($\langle\ldots\rangle$) is taken over the distribution function of the beam; recall also (1.27–1.29). An analoguous expression holds for the vertical plane. For a coupled system, the general form of (4.1) must be taken.

Control of the beam emittance and prevention of emittance dilutions are mandatory for achieving high brilliance in light sources and high luminosity in colliding beam accelerators. Some sources of emittance dilution, e.g., beam-gas scattering, are inevitable and can be reduced only via hardware improvements. In the same vane, processes involving space-charge dilutions, which constitute a predominant limitation for low-energy ion or proton beams, have after-the-observation been treated by fundamental changes in the acceleration optics, as illustrated, e.g., by the FNAL linac upgrade, and a new booster ring at BNL. Another class of dilutions involving man-made sources, e.g., component vibration, ground motion, power supply regulation, etc., may be curable using sophisticated measurement devices and feedback or feedforward schemes. In this case, the crucial ingredient leading to improved performance is the detection of the offending presence, e.g., using model-independent analysis, as discussed in Chap. 2, or more commonly analyses in the frequency domain.

An interesting example of the latter case is shown in Fig. 4.1. Plotted is the Fourier transform of pulse-by-pulse BPM measurements from the SLC linac. The data evidence a strong component at about 1 Hz which seemed

M. G. Minty et al., *Measurement and Control of Charged Particle Beams,*
https://doi.org/10.1007/978-3-662-08581-3_4

to partly explain the 1 Hz 'wave' in the backgrounds recorded by the SLD detector. However, at this time, the data acquisition was limited to 30 Hz (with a beam repetition frequency of 120 Hz). As a result, the sampled data were aliased; that is, the Fourier line appearing at 1 Hz corresponded actually to 59 Hz as verified later with a faster (120 Hz) data acquisition speed. The source of these excitations was eventually traced back to asynchronous (to the beam) operation of the cooling water pumps for the linac quadrupoles. Once the disturbance was identified[1], corresponding measures were implemented – in this case, damping of the vibrations resulting from the turbulent water flow and modifications to the pump impellers – and the impact on the beam was correspondingly reduced. Identification of the error sources evidenced by the remaining peaks in Fig. 4.1 was also partially successful [1].

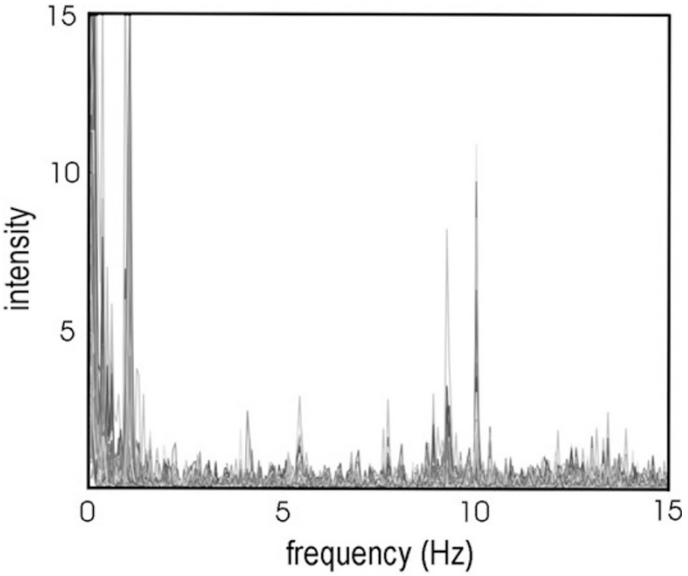

Fig. 4.1. Frequency spectrum of beam motion in the SLC linac, revealing the contribution of water pumps operating at 59 Hz [1]

Other common situations which lead to emittance dilutions arise from poor setting of the accelerator including poor "matching" between accelerator subsystems, residual betatron coupling (which may also be caused by unknown field errors), or spurious dispersion which arises either directly from magnet misalignments or from imperfect attempts to correct for alignment errors by one-to-one steering. The latter may arise from insufficient knowledge of the accelerator optics (as limited by the BPM resolution, for example) or

[1] which proved difficult since in fact there actually was at that time a 1 Hz component on the beam introduced incorrectly by the orbit feedback loops as these also reacted on the aliased frequency

may arise intrinsically from the alignment procedure itself (as is the case, e.g., of using the one-to-one steering algorithm).

Finally, there are processes which are in practice hard to predict that also lead to emittance dilutions. Such processes, predominant especially with high beam intensities, include, at high single-bunch charge both transverse and longitudinal wakefields effects leading to beam instabilities in circular accelerators and to beam centroid excursions in linear accelerators, and at high single-bunch charge and high total current also beam instabilities arising from ions or electron clouds.

In all the above cases, the diagnosis is precedented by an accurate measurement of the beam emittance. In this chapter, standard emittance measurement techniques will be outlined in a step-by-step manner. Then some methods used to minimize the beam emittance by changing the underlying accelerator optics will be reviewed.

4.1 Beam Emittance Measurements

In this section we describe not single particle transport, but transport of the beam as a whole. The beam quality will be characterized by the beam emittance which is often measured with reference to a particular plane of interest; i.e., the horizontal, vertical, or longitudinal emittance. Methods for measuring the beam emittance and for parametrizing the degree of mismatch will be outlined.

We note that many novel measurement techniques have recently been developed for measuring very small beam sizes including interferometric methods, applied in the beamline at the SLAC final focus test facility [2] or in the ATF damping ring [3], or tomographic phase space reconstruction applied at the TTF linac [4]. A recent review of similar topics is given in [5]. In this section we restrict the discussion to emittance measurement techniques, which are based on commonly used and relatively simple hardware. For illustration we describe measurements and present experimental data obtained using wire scanners although the measurement principles have been similarly applied with the use of fluorescent screens.

4.1.1 Single Wire Measurement

The beam emittance can be measured by varying the field strength of a quadrupole located upstream of a single wire or screen. In general this will lead to trajectory and beam-size changes downstream, and, hence, is referred to as an "invasive" measurement. The measurement could be made less invasive by simultaneously adjusting another quadrupole downstream of the wire scanner, so as to compensate for the change in the beta function induced by the first quadrupole. This has been rarely done in the past, but is a proposed scheme for future linear colliders.

The total transfer matrix of interest here is $R = SQ$, where S denotes the known transfer matrix between the quadrupole and the wire, and Q is the transfer matrix of the quadrupole:

$$Q = \begin{pmatrix} 1 & 0 \\ K & 1 \end{pmatrix} , \tag{4.3}$$

where we have invoked the thin-lens approximation, which is valid if the length of the quadrupole is short compared to its focal length $f = 1/K$. After matrix multiplication, one obtains

$$R = \begin{pmatrix} S_{11} + KS_{12} & S_{12} \\ S_{21} + KS_{22} & S_{22} \end{pmatrix} , \tag{4.4}$$

where the coefficients S_{ij} are the components of the matrix S. Expanding the matrix product for the 2×2 beam matrix $\Sigma^x_{\text{beam}} = (SQ)\Sigma^x_{\text{beam},0}(SQ)^T$ and equating the (1,1) elements on both sides, the square of the horizontal beam size follows as

$$\begin{aligned} \Sigma_{11}(= \langle x^2 \rangle) = {} & ({S_{11}}^2 \Sigma_{11_0} + 2S_{11}S_{12}\Sigma_{12_0} + {S_{12}}^2 \Sigma_{22_0}) \\ & + (2S_{11}S_{12}\Sigma_{11_0} + 2{S_{12}}^2 \Sigma_{12_0})K + {S_{12}}^2 \Sigma_{11} K^2 , \end{aligned} \tag{4.5}$$

which is quadratic in the field parameter K.

To make use of these results in an emittance measurement, the following procedure is often employed:

1. For each value of quadrupole field strength K, the wire is scanned and the amplitude of the response measured by a detector is obtained as a function of wire position.
2. For each wire scan at fixed K, the distribution is fitted with a Gaussian of the form

$$f(x) = f_0 + f_{\max} e^{-\frac{(x - \langle x \rangle)^2}{2\langle x^2 \rangle}} , \tag{4.6}$$

where f_0 is the baseline level offset and $f_{\max}$ is the peak value of the Gaussian distribution.
3. The fitted beam size $\langle x^2 \rangle$ is plotted as a function of K.
4. The result is fitted with a parabola. One parametrization for the fit [6] is

$$\begin{aligned} \Sigma_{11} &= A(K - B)^2 + C \\ &= AK^2 - 2ABK + (C + AB^2) . \end{aligned} \tag{4.7}$$

5. The Σ matrix is reconstructed by equating coefficients of (4.5) and (4.7):

$$A = S_{12}^2 \Sigma_{11} , \tag{4.8}$$

$$-2AB = 2S_{11}S_{12}\Sigma_{11} + 2S_{12}^2 \Sigma_{12} , \tag{4.9}$$

$$C + AB^2 = {S_{11}}^2 \Sigma_{11} + 2S_{11}S_{12}\Sigma_{12} + {S_{12}}^2 \Sigma_{22} , \tag{4.10}$$

and solving for Σ_{11}, Σ_{12} $(= \Sigma_{21})$, and Σ_{22}. The results are

$$\Sigma_{11} = A/{S_{12}}^2 \,, \tag{4.11}$$

$$\Sigma_{12} = -\frac{A}{{S_{12}}^2}\left(B + \frac{S_{11}}{S_{12}}\right) \,, \tag{4.12}$$

$$\Sigma_{22} = \frac{1}{{S_{12}}^2}\left[(AB^2 + C) + 2AB\left(\frac{S_{11}}{S_{12}}\right) + A\left(\frac{S_{11}}{S_{12}}\right)^2\right] \,. \tag{4.13}$$

6. The beam emittance is then calculated from the determinant of the beam matrix $\epsilon_x = \sqrt{\det\, \Sigma^x_{\rm beam}}$ and the errors are propagated:

$$\det\, \Sigma^x_{\rm beam} = \Sigma_{11}\Sigma_{22} - {\Sigma_{12}}^2 \tag{4.14}$$

$$= AC/S_{12}^4 \,, \tag{4.15}$$

so that

$$\epsilon_x = \sqrt{AC}/S_{12}^2 \,. \tag{4.16}$$

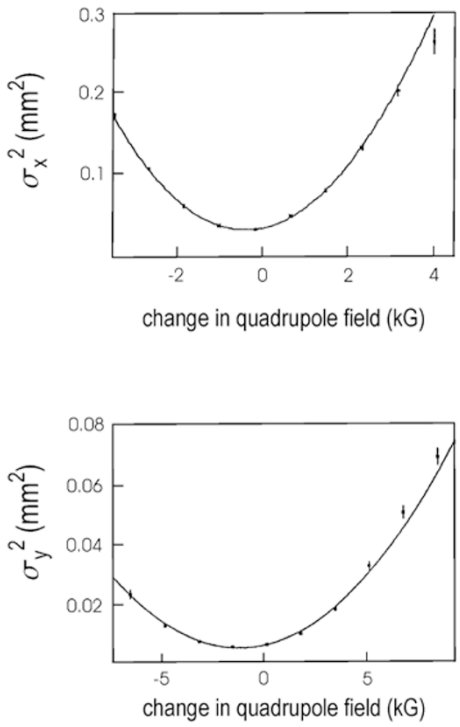

Fig. 4.2. Example transverse beam emittance measurements from the SLC prior to injection into the main linac using a single wire. The fit parameters for the horizontal emittance (*top*) were $A = 3494 \pm 52$, $B = -118.8 \pm 0.03$, $C = 3.2 \times 10^4 \pm 297$ with $\chi^2/\mathrm{dof} = 1.5$ giving $\epsilon_x = 12.9 \pm 0.2$ nm-rad or $\gamma\epsilon_x = 30.1 \pm 0.4$ μm-rad. In the vertical plane (*bottom*), $A = 158.5 \pm 3.5$, $B = -129.3 \pm 0.08$, and $C = 5.1 \times 10^3 \pm 103$ with $\chi^2/\mathrm{dof} = 4.6$ giving $\epsilon_y = 1.71 \pm 0.02$ nm-rad or $\gamma\epsilon_x = 3.98 \pm 0.04$ μm-rad

The above results also give the beam-ellipse parameters α_x, β_x, and γ_x:

$$\beta_x = \frac{\Sigma_{11}}{\epsilon} = \sqrt{\frac{A}{C}}\,, \tag{4.17}$$

$$\alpha_x = -\frac{\Sigma_{12}}{\epsilon} = \sqrt{\frac{A}{C}}\,\left(B + \frac{S_{11}}{S_{12}}\right)\,, \tag{4.18}$$

$$\gamma_x = \frac{{S_{12}}^2}{\sqrt{AC}}\left[(AB^2 + C) + 2AB\left(\frac{S_{11}}{S_{12}}\right) + A\left(\frac{S_{11}}{S_{12}}\right)^2\right]\,. \tag{4.19}$$

As a useful check, the beam-ellipse parameters should satisfy $(\beta_x\gamma_x - 1) = \alpha_x^2$.

An example of emittance measurements in the two transverse planes x and y is shown in Fig. 4.2. Notice that the optics at the wire scanners has been optimally chosen to allow simultaneous measurement of the beam waists in both transverse planes.

4.1.2 Multiple Wire Measurement

The beam emittance in a transport line or linac may be measured (in many applications noninvasively) using multiple wire scanners. Here, the quadrupole gradients are fixed, but the R matrices between s_0 and the different wire scanners (or other beam-size monitors) are different. If there are no coupling elements, three measurements using three wire scanners are required. With coupling, four wire scanners are needed (in this case each wire scanner should be equipped with several wires oriented at different angles in the transverse plane, e.g., a horizontal, a vertical and a wire oriented at 45° in the case of 'round beams' with equal horizontal and vertical beam size). The optimum wire locations for maximum sensitivity (without coupling) are such that the separation between wires corresponds to a difference in betatron phase advance $\Delta\mu$ of $90°/N_w$, where N_w is the number of wires used in the measurement.

The matrix equation to be solved is

$$\begin{pmatrix} (\sigma_x{}^{(1)})^2 \\ (\sigma_x{}^{(2)})^2 \\ (\sigma_x{}^{(3)})^2 \\ \cdots \\ (\sigma_x{}^{n})^2 \end{pmatrix} = \begin{pmatrix} (R_{11}{}^{(1)})^2 & 2R_{11}^{(1)}R_{12}^{(1)} & (R_{12}{}^{(1)})^2 \\ (R_{11}{}^{(2)})^2 & 2R_{11}^{(2)}R_{12}^{(2)} & (R_{12}{}^{(2)})^2 \\ (R_{11}{}^{(3)})^2 & 2R_{11}^{(3)}R_{12}^{(3)} & (R_{12}{}^{(3)})^2 \\ & \cdots & \\ (R_{11}{}^{(n)})^2 & R_{11}^{(n)}R_{12}^{(n)} & (R_{12}{}^{(n)})^2 \end{pmatrix} \begin{pmatrix} \beta(s_0)\epsilon \\ -\alpha(s_0)\epsilon \\ \gamma(s_0)\epsilon \end{pmatrix}\,. \tag{4.20}$$

This equation is applicable for both a multiple wire measurement or for a quadrupole scan. The superindex within parenthesis refers to the different different measurements; i.e., it either corresponds to the setting of some quadrupole magnet, in the case of a quadrupole scan, or to a different wire scanner or monitor, in the case of a multi-wire emittance measurement. The

superindex '2' is meant to denote the square of the quantity. At least 3 measurements are required in order to solve for the three independent parameters ϵ, $\beta(s_0)$ and $\alpha(s_0)$.

To simplify the notation, let us denote the $n \times 3$ matrix on the right-hand side of (4.20) as $\mathbf{B}$, the n-component vector on the left side by $\Sigma_x = (\sigma_x^{(1)2}, ..., \sigma_x^{(n)2})$, and the 3-component vector on the far right by

$$\mathbf{o} = (\beta(s_0)\epsilon, -\alpha(s_0)\epsilon, \gamma(s_0)\epsilon)\,. \tag{4.21}$$

The equation is then

$$\Sigma_x = \mathbf{B} \cdot \mathbf{o}\,. \tag{4.22}$$

The problem of determining the elements of the vector $\mathbf{o}$ can be solved by a simple least-squares fit. We have to minimize the sum

$$\chi^2 = \sum_{l=1}^{n} \frac{1}{\sigma^2_{\Sigma_x^{(l)}}} \left(\Sigma_x^{(l)} - \sum_{i=1}^{3} B_{li} o_i \right)^2 , \tag{4.23}$$

where $\sigma_{\Sigma_x^{(l)}}$ denotes the rms error of $\Sigma_x^{(l)} = \sigma_x^{(l)2}$. This error is obtained from the fit to the lth wire scan which determines the rms beam size $\sigma_x^{(l)}$.

We find it convenient to normalize the coordinates $\Sigma^{(l)}$ so that the rms error is 1, introducing

$$\hat{\Sigma}_x^{(l)} = \frac{\Sigma_x^{(l)}}{\sigma_{\Sigma_x^{(l)}}}\,, \tag{4.24}$$

and

$$\hat{B}_{li} = \frac{B_{li}}{\sigma_{\Sigma_x^{(l)}}}\,. \tag{4.25}$$

Forming a symmetric $n \times n$ covariance matrix

$$\mathbf{T} = (\hat{\mathbf{B}}^t \cdot \hat{\mathbf{B}})^{-1}\,, \tag{4.26}$$

the least-squares solution to (4.22) is

$$\mathbf{o} = \mathbf{T} \cdot \hat{\mathbf{B}}^t \cdot \hat{\Sigma}_x\,, \tag{4.27}$$

and the error of any scalar function $f(\mathbf{o})$ is given by

$$\sigma(f)^2 = (\nabla_{\mathbf{o}} f)^t \cdot \mathbf{T} \cdot (\nabla_{\mathbf{o}} f)\,. \tag{4.28}$$

In particular, the errors of the parameters $\mathbf{o}$ themselves are

$$\sigma_{o_i} = \sqrt{T_{ii}}\,. \tag{4.29}$$

Once the components of $\mathbf{o}$ are known, we still need to perform a simple nonlinear transformation to infer ϵ, β, and α:

$$\epsilon = \sqrt{o_1 o_3 - o_2^2}\,, \tag{4.30}$$

$$\beta = o_1/\epsilon\,, \text{ and} \tag{4.31}$$

$$\alpha = -o_2/\epsilon\,. \tag{4.32}$$

The error propagation is straightforward, using (4.28).

A possible procedure for the multiple wire emittance measurement is as follows:
1. Each wire is scanned to obtain detector counts versus wire position x.
2. For each wire scan, the distribution is fit with a Gaussian using (4.6).
3. The Σ matrix is reconstructed using (4.20), the transfer matrix elements R_i from the model, and the σ_i from the measurements.
4. The emittance is calculated $\epsilon = \sqrt{\det \Sigma_{\text{beam}}}$.
5. The ellipse parameters $\alpha = -\Sigma_{12}/\epsilon$, $\beta = \Sigma_{11}/\epsilon$, and $\gamma = \Sigma_{22}/\epsilon$ are calculated, if desired.

4.1.3 Graphics

Increased operational efficiency may be obtained from a meaningful graphical representation of the experimental data. In the multiple wire emittance measurement it is useful to project the measurements to a single point along the accelerator and to plot the normalized phase space. The emittance ϵ, multiplied by π, corresponds to the area of the ellipse parametrized by

$$\epsilon = \gamma_x x^2 + 2\alpha_x x x' + \beta_x {x'}^2\,. \tag{4.33}$$

Since $\beta\gamma = 1 + \alpha^2$,

$$\epsilon = \frac{1}{\beta_x}[x^2 + (\alpha_x x + \beta_x x')^2] = \frac{1}{\beta_x}(x^2 + {p_x}^2)\,, \tag{4.34}$$

where $p_x = \alpha_x x + \beta_x x'$ is the coordinate orthogonal to x.

A succinct representation of the measured beam emittances is obtained by the following procedure (applied at the SLC), which displays the data in the normalized phase space, so that deviations from the design values are immediately obvious. The wire orientations are also plotted to indicate the phase space coverage provided by the wires:
1. Plot the design rms ellipse in the coordinates

$$\left(\frac{x}{\sqrt{\beta_x}}, \frac{\alpha_x x + \beta_x x'}{\sqrt{\beta_x}}\right) \tag{4.35}$$

at some reference point s along the trajectory. This results in a circle. Normalize the design ellipse to unit radius.
2. Plot also the ellipse obtained from the measurements of the ellipse parameters transposed to the reference point. Apply the same normalization as in step 1.

3. Using the lattice model, project each beam-size measurement back to the reference point and add the result as a line to the figure; that is, for each point $(\sigma_{x,w}, x'_w)$, where $\sigma_{x,w}$ is the beam size measured at the wire, apply an inverse mapping to the reference point:

$$\begin{pmatrix} x \\ x' \end{pmatrix}_{\text{ref point}} = R^{-1} \begin{pmatrix} \sigma_{x,w} \\ x'_w \end{pmatrix} , \tag{4.36}$$

where R is the 2×2 transport matrix from the reference point to the location of the wire. Here x'_w represents the undetermined angle variable (divergence) at the wire which parametrizes the location along the straight line in the phase space defined by (4.35). The slope of this line is related to the phase advance between the reference point and the wire.

An accompanying display of numbers should summarize the measurements which might include the measured and expected beam widths at each of the wires, the measured and design beam emittances, as well as the beam intensity. In addition, a measure of the degree of "mismatch" is useful. This will be further discussed in the next section.

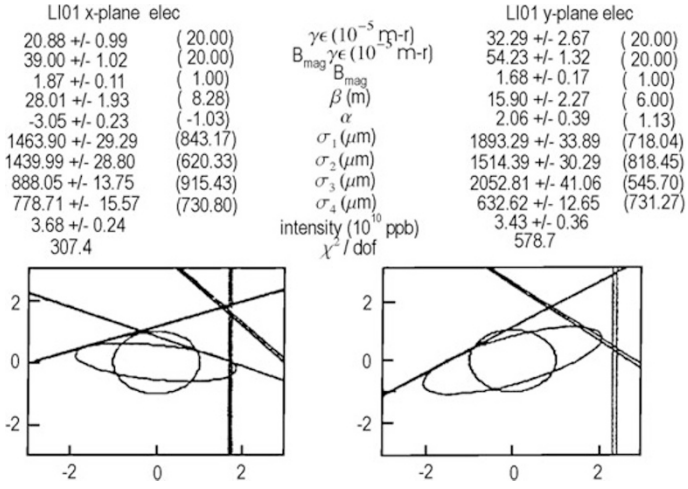

Fig. 4.3. Graphics output of multiple-wire transverse beam emittance measurement in the injector linac at the SLC

An example of this graphics is shown in Fig. 4.3. The corresponding raw data are given in Fig. 4.4. From Fig. 4.3 it is immediately obvious that while the measured ellipse has roughly the same emittance as the design circle (the horizontal emittance is 208.8 ± 9.9 [mm-mrad] compared to the design of 200 [mm-mrad], the vertical emittance is 323 ± 26.7 [mm-mrad] compared to the design of 200 [mm-mrad]), the ellipse orientation is incorrect. As will be shown in the next section, if this beam were allowed to propagate uncorrected,

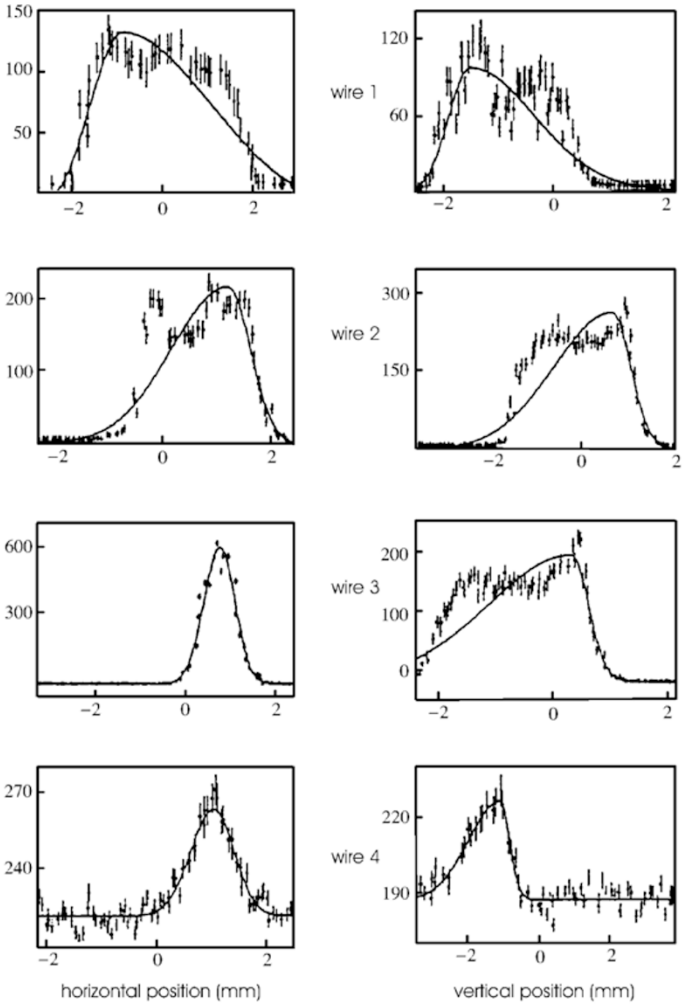

Fig. 4.4. Raw data showing individual wire scans used in the summary display of Fig. 4.3 and the "asymmetric Gaussian" fits of (4.37)

the final emittance titled $B_{mag}\epsilon$ would be 390.0 ± 10.2 [mm-mrad] in x and 543.3 ± 13.2 [mm-mrad] in y. The emittance dilution factor B_{mag} represents the degree of the mismatch. From Fig. 4.3 can be deduced immediately the degree of phase space coverage spanned by the wires. In the horizontal plane, for example, the wire orientations are about $0°$, $-45°$, $-22.5°$, and $-67.5°$, which is ideal for a 4-wire emittance measurement.

The "measured ellipse", that is the ellipse that was reconstructed from the beam widths obtained by Gaussian fits to the individual wire scans, does not always represent the true rms emittance of a Gaussian beam distribution.

This can be seen by inspecting the raw data shown in Fig. 4.4. For more complex beam distributions, a somewhat better characterization is achieved by applying an "asymmetric Gaussian" fit to the wire-scan measurement, in which the left and right hand sides of the measured beam profile are approximated independently by two separate Gaussians. For example, the fitting function used at the SLC [7] was

$$f(x) = f_0 + f_{\max} \exp\left[-\frac{(x - \langle x\rangle)^2}{2\langle x^2\rangle(1 + \alpha[\mathrm{sign}(x - \langle x\rangle)]}\right], \tag{4.37}$$

where α represents an asymmetry factor and is zero for a perfect Gaussian[2]. The σ for the left and right hand sides of the fitted distribution are $\sigma = \langle x^2\rangle(1 \pm \alpha)$. For the ellipse reconstruction the average σ was used. When large tails are present in the raw data this more accurately represents the beam distribution. Based on the raw data it is clear, however, that even with the more sophisticated fitting algorithm, the fit only marginally represents the actual distributions.

For reasonably well "matched" beams, the graphical summary display is most useful for quick evaluation of the beam. In this example the deviations between the design and measured ellipse in the graphics suggest that a closer inspection of the raw data may be warranted. The "double-humps" in the single-wire measurements are characteristic of an upstream error; a beam, if kicked transversely, will filament, i.e., it loses coherency due to the natural spread in the phase advance between particles, resulting in an increased emittance and the characteristic double humps.

If a wire is mounted at 45° with respect to x and y (a "u-plane" wire), then it is also possible to measure the coupling between the horizontal and vertical plane. The (4×4) Σ-matrix is

$$\Sigma^{xy}_{\mathrm{beam}} = \begin{pmatrix} \Sigma_{11} & \Sigma_{12} & \Sigma_{13} & \Sigma_{14} \\ \Sigma_{21} & \Sigma_{22} & \Sigma_{23} & \Sigma_{24} \\ \Sigma_{31} & \Sigma_{32} & \Sigma_{33} & \Sigma_{34} \\ \Sigma_{41} & \Sigma_{42} & \Sigma_{43} & \Sigma_{44} \end{pmatrix}, \tag{4.38}$$

where, for example, Σ_{14} represents the correlation between x and y'. Notice that $\Sigma_{14} \neq \Sigma_{23}$. Whereas for the single plane uncoupled beam matrix reconstruction a minimum of 3 measurements are required, to fully reconstruct the coupled beam matrix a total of 10 measurements is needed. This includes the 3 measurements in the x plane, 3 in the y plane, and 4 in the u plane. The raw data used in such a coupled emittance measurement is presented in Figs. 4.5–4.7. In this case the raw data are well fitted using Gaussian fits. From these fits, using the uncoupled analysis (with only the x and y wires) presented previously, $\gamma\epsilon_x = (2.20 + / - 0.01) \times 10^{-5}$ m-r and

[2] with high resolution scanners this parameter may also prove useful for characterizing 'banana' beams in future linear colliders

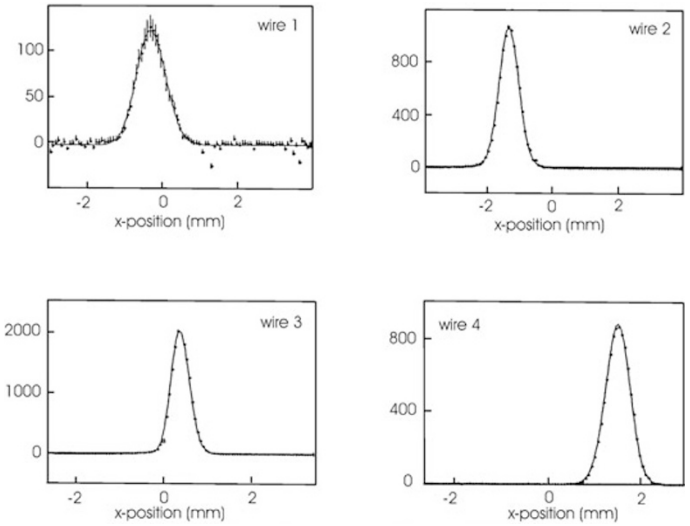

Fig. 4.5. Raw data in the x-plane for emittance measurement with $x - y$ coupling

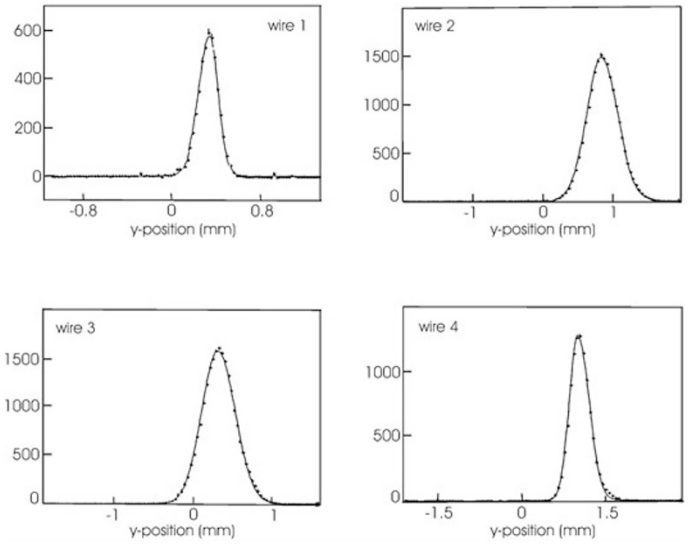

Fig. 4.6. Raw data in the y-plane for emittance measurement with $x - y$ coupling

$\gamma\epsilon_y = (1.89 + / - 0.02) \times 10^{-5}$ m-r. Using the complete data set, and projecting the distributions onto the eigenplanes of the tilted beam ellipses, the fits yielded $\gamma\epsilon_1 = 2.13 \times 10^{-5}$ m-r and $\gamma\epsilon_2 = 1.71 \times 10^{-5}$ m-r, which is in reasonable agreement with the results obtained excluding coupling effects indicating that the coupling is small. However, the error bars were not fully propagated. Recent experience at the ATF has shown that proper wire orientations are

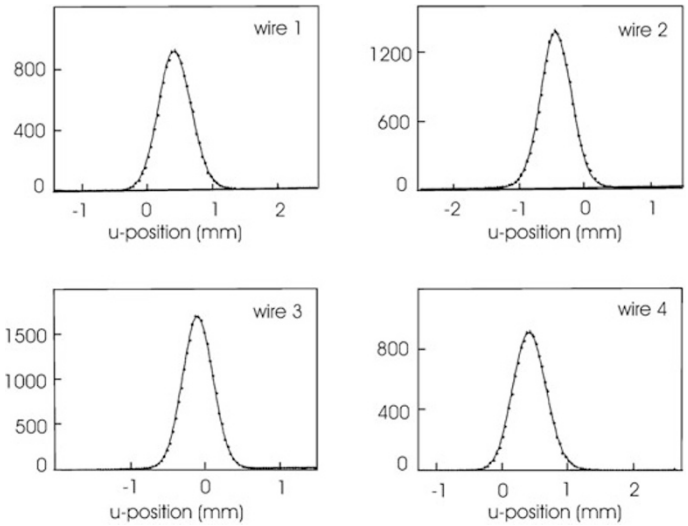

Fig. 4.7. Raw data in the u-plane for emittance measurement with $x - y$ coupling

critical for maximizing sensitivity particularly for flat beam measurements. Moreover, measurement errors can strongly influence the value of the emittance [8] interpreted from the approach given above. More robust tuning procedures for minimizing the linear coupling are given in [8].

4.1.4 Emittance Mismatch

In this section we begin by explicitly computing, in two dimensions, the transverse position and angle using the general form of the beam transfer matrix for a periodic lattice. This result is used to calculate the individual elements of the beam transfer matrix and to derive an expression for the mismatch parameter $\mathrm{B_{mag}}$ [9, 10].

The parameter $\mathrm{B_{mag}}$ has an important physical meaning. If a beam is injected into a ring or linac with a mismatch, the beam will filament until its distribution approaches a shape that is matched to the ring or the linac lattice. However, the filamentation causes the beam emittance to increase, such that, after complete filamentation, the emittance is given by the product of $\mathrm{B_{mag}}$ and the initial value of ϵ. The mismatch parameter is well suited for analysis in circular machines for which the periodicity is implicit. We will see that the same formalism is useful in describing emittance transport in linear accelerators and transport lines as well.

Derivation of Beam Matrix Elements. According to (1.27) and after subtracting the mean values from all coordinates, the beam matrix is

$$\Sigma^x_{\mathrm{beam}} = \begin{pmatrix} \langle x^2 \rangle & \langle xx' \rangle \\ \langle xx' \rangle & \langle x'^2 \rangle \end{pmatrix}. \tag{4.39}$$

From (1.25), the point-to-point transfer matrix is

$$R_{fi} = \begin{pmatrix} \sqrt{\frac{\beta_f}{\beta_i}}(\cos\phi_{fi} + \alpha_i \sin\phi_{fi}) & \sqrt{\beta_f\beta_i}\sin\phi_{fi} \\ \frac{\alpha_i - \alpha_f}{\sqrt{\beta_f\beta_i}}\cos\phi_{fi} - \frac{1+\alpha_f\alpha_i}{\sqrt{\beta_f\beta_i}}\sin\phi_{fi} & \sqrt{\frac{\beta_i}{\beta_f}}(\cos\phi_{fi} - \alpha_f\sin\phi_{fi}) \end{pmatrix}, \tag{4.40}$$

where α_f and β_f are the ellipse parameters at a (final) observation point f downstream of a reference point, which is denoted by the subscript i. Here ϕ_{fi} is the phase advance between the reference point and the observation point and is equal to

$$\phi_{fi} = \int_{s_i}^{s_f} \frac{\mathrm{d}s}{\beta}\,. \tag{4.41}$$

For a periodic lattice for which $\alpha = \alpha_0$ and $\beta = \beta_0$, the periodic, one turn map, transfer matrix R_{otm} is given by (1.26):

$$R_{\mathrm{otm}} = \begin{pmatrix} \cos\mu + \alpha\sin\mu & \beta\sin\mu \\ -\gamma\sin\mu & \cos\mu - \alpha\sin\mu \end{pmatrix}. \tag{4.42}$$

The beam matrix elements after 1 iteration through the periodic lattice are

$$\langle x^2\rangle_n = \langle x^2\rangle_0 {R_{11}}^2 + 2\langle xx'\rangle_0 R_{11}R_{12} + \langle x'^2\rangle_0 {R_{12}}^2\,, \tag{4.43}$$

$$\langle xx'\rangle_n = \langle x^2\rangle_0 R_{11}R_{21} + \langle xx'\rangle_0[R_{11}R_{22} + R_{12}R_{21}] + \langle x'^2\rangle_0 R_{12}R_{22}\,, \tag{4.44}$$

$$\langle x'^2\rangle_n = \langle x^2\rangle_0 {R_{21}}^2 + 2\langle xx'\rangle_0 R_{21}R_{22} + \langle x'^2\rangle_0 {R_{22}}^2\,. \tag{4.45}$$

After substitution of the matrix elements of (4.42) into (4.44–4.45), and using $\cos 2\psi = \cos^2\psi - \sin^2\psi$ and $\sin 2\psi = 2\sin\psi\cos\psi$,

$$\begin{aligned} \langle x^2\rangle_n &= \frac{1}{2}[\langle x^2\rangle_0 + \langle(\alpha x_0 + \beta x_0')^2\rangle] \\ &\quad - \frac{1}{2}[\langle x^2\rangle_0\left(\alpha^2 - 1\right) + 2\beta\alpha\langle xx'\rangle_0 + \beta^2\langle x'^2\rangle_0]\cos 2\psi \\ &\quad + [\alpha\langle x^2\rangle_0 + \beta\langle xx'\rangle_0]\sin 2\psi\,, \end{aligned} \tag{4.46}$$

$$\begin{aligned} \langle x'^2\rangle_n &= \frac{1}{2}[\langle x'^2\rangle_0 + \langle(\alpha x' + \gamma x)^2\rangle_0] \\ &\quad + \frac{1}{2}[\langle x'^2\rangle_0 - \langle(\alpha x' + \gamma x)^2\rangle_0]\cos 2\psi \\ &\quad - [\alpha\langle x'^2\rangle_0 + \gamma\langle xx'\rangle_0]\sin 2\psi\,, \end{aligned} \tag{4.47}$$

$$\begin{aligned} \langle xx'\rangle_n &= \frac{1}{2}[-\alpha\gamma\langle x^2\rangle_0 - 2\alpha\langle xx'\rangle_0 - \alpha\beta\langle x'^2\rangle_0] \\ &\quad + \left[\frac{\alpha\gamma}{2}\langle x^2\rangle_0 + (1+\alpha^2)\langle xx'\rangle_0 + \frac{\alpha\beta}{2}\langle x'^2\rangle_0\right]\cos 2\psi \\ &\quad + \frac{1}{2}[-\gamma\langle x^2\rangle_0 + \beta\langle x'^2\rangle_0]\sin 2\psi\,. \end{aligned} \tag{4.48}$$

Next, let

$$a = \frac{\beta}{2}[\gamma\langle x^2\rangle_0 + 2\alpha\langle xx'\rangle_0 + \beta\langle x'^2\rangle_0]\,, \tag{4.49}$$

$$b = \frac{\gamma}{\beta}a\,, \tag{4.50}$$

$$c = -\frac{\alpha}{\beta}a\,, \tag{4.51}$$

and use

$$c_1\cos 2\psi + c_2\sin 2\psi = \sqrt{{c_1}^2 + {c_2}^2}\cos(2\psi - \chi),\ \text{with}\ \chi = \tan^{-1}\left(\frac{c_2}{c_1}\right). \tag{4.52}$$

Then,

$$\langle x^2\rangle_n = a + \sqrt{a^2 - \beta^2(\langle x^2\rangle_0\langle x'^2\rangle_0 - \langle xx'\rangle_0{}^2)}\cos(2\psi + \chi_{\langle x^2\rangle_0})\,, \tag{4.53}$$

$$\langle x'^2\rangle_n = b + \sqrt{b^2 - \gamma^2(\langle x^2\rangle_0\langle x'^2\rangle_0 - \langle xx'\rangle_0{}^2)}\cos(2\psi + \chi_{\langle x'^2\rangle_0})\,, \tag{4.54}$$

and

$$\langle xx'\rangle_n = c + \sqrt{(\langle xx'\rangle_0 - c)^2 + \left(-\frac{\gamma}{2}\langle x^2\rangle_0 + \frac{\beta}{2}\langle x'^2\rangle_0\right)^2}\cos(2\psi + \chi_{\langle xx'\rangle_0})\,, \tag{4.55}$$

where the angles $\chi_{\langle x^2\rangle_0}$, $\chi_{\langle x'^2\rangle_0}$, and $\chi_{\langle xx'\rangle_0}$, follow from (4.52), (4.46), (4.47), and (4.48), respectively. Note that since $\epsilon = \sqrt{\det\sigma}$ is an invariant in the absence of filamentation,

$$\langle x^2\rangle_n\langle x'^2\rangle_n - \langle xx'\rangle_n^2 = \langle x^2\rangle_0\langle x'^2\rangle_0 - \langle xx'\rangle_0^2\,. \tag{4.56}$$

The Mismatch Parameter [9] $\mathrm{B_{mag}}$. Dividing both sides of (4.53) by $\beta\epsilon_0 = \beta\sqrt{\langle x^2\rangle_0\langle x'^2\rangle_0 - \langle xx'\rangle_0}$, we have

$$\begin{aligned}\frac{\langle x^2\rangle_n}{\beta\epsilon_0} &= \frac{a/\beta}{\sqrt{\langle x^2\rangle_0\langle x'^2\rangle_0 - \langle xx'\rangle_0{}^2}} \\ &\quad + \sqrt{\left(\frac{a/\beta}{\sqrt{\langle x^2\rangle_0\langle x'^2\rangle_0 - \langle xx'\rangle_0{}^2}}\right)^2 - 1}\ \cos(2\psi - \chi_{\langle x^2\rangle_0}) \\ &= \mathrm{B_{mag}} + \sqrt{\mathrm{B_{mag}^2} - 1}\cos(2\psi - \chi_{\langle x^2\rangle_0})\,,\end{aligned} \tag{4.57}$$

where the mismatch parameter $\mathrm{B_{mag}}$ is defined as

$$\mathrm{B_{mag}} = \frac{a/\beta}{\sqrt{\langle x^2\rangle_0\langle x'^2\rangle_0 - \langle xx'\rangle_0}}\,. \tag{4.58}$$

With the ellipse parameters α, β, and γ referring to the steady-state or equilibrium beam distribution, we have

$$\mathrm{B_{mag}} = \frac{1}{2}\frac{[\gamma\langle x^2\rangle_0 + 2\alpha\langle xx'\rangle_0 + \beta\langle x'^2\rangle_0]}{\sqrt{\langle x^2\rangle_0\langle x'^2\rangle_0 - \langle xx'\rangle_0}}\,. \tag{4.59}$$

Thus, $\mathrm{B_{mag}}$ is the ratio of the area of the decohered beam to the area of the injected beam. The factor of 2 results from the numerator representing an rms area.

Examples of Emittance Dilution due to Mismatch. Emittance dilution results if $\mathrm{B_{mag}} \neq 1$ due to the difference in the transverse phase advance of the particles within the bunch. There are multiple sources of such phase advance variations. The two most commonly considered sources depend on the chromaticity or on the amplitude of the betatron oscillations. The chromaticity ξ $(\equiv Q'/Q) = (\Delta\psi/\psi)/\delta$ characterizes the energy dependence of the phase advance where $\Delta\psi$ is the difference in the phase advance of a particle from the mean phase advance of the bunch and δ is the relative energy deviation of that particle compared to the mean energy of the bunch. The amplitude dependence of the phase advance due to sextupole or octupolar magnetic fields is approximately described by

$$2\pi\psi = 2\pi\psi_0 - \mu a^2\,, \tag{4.60}$$

where ψ_0 is the phase advance for a reference particle on the closed orbit, μ characterizes the strength of the sextupolar or octupolar fields, and a is the betatron oscillation amplitude of the particle. Less commonly considered sources for phase advance variations include wakefield focussing or space-charge defocussing for high current beams, focussing due to ions or electron clouds, and focussing due to the beam-beam tune shift in colliding beam accelerators.

a) Periodic Lattice

Let the length of the lattice period be L. Then, as shown in Fig. 4.8, for $\mathrm{B_{mag}} = 1$, the beam always fills the same area in phase space after each lattice period. The rms area of the ellipse after n turns is

$$\langle x^2\rangle_n = \beta\epsilon_0\,, \tag{4.61}$$

and the beam is said to be matched. Under these conditions, no emittance dilution will occur. In particular, since $\langle x^2\rangle_n$ is independent of the phase advance ψ, the phase space area is unchanged even if the phase of each of the particles in the beam advances differently.

For $\mathrm{B_{mag}} > 1$, then

$$\begin{aligned}\epsilon_n &= \frac{\langle x^2\rangle_n}{\beta} \\ &= \epsilon_0\left[\mathrm{B_{mag}} + \sqrt{\mathrm{B_{mag}}^2 - 1}\cos(2\psi - \chi_{\langle x^2\rangle_0})\right]\,,\end{aligned} \tag{4.62}$$

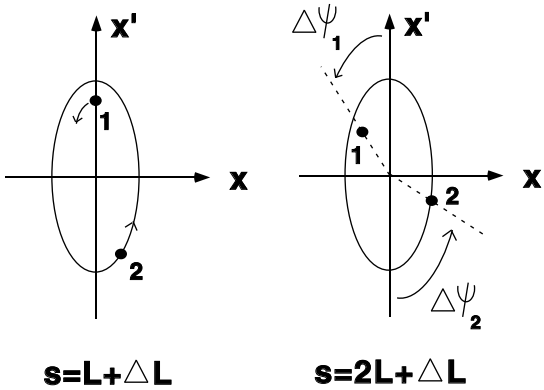

Fig. 4.8. Horizontal phase space for a matched beam in a periodic lattice. The emittance is preserved even if the phase advance is different for different particles (denoted here by the numbers 1 and 2)

as shown in Fig. 4.9. The solid, small ellipse represents the matched ellipse for which $B_{mag} = 1$. The shaded ellipse represents the (1σ) rms distribution of the mismatched beam. During the first few traversals of identical lattice segments, the phase advance variations of the different particles may not be obvious. As n approaches infinity, however, the phase advance variations lead to a smearing in the transverse phase space resulting in a larger emittance. This is represented by the area occupied by the hatched ellipse as given by (4.57).

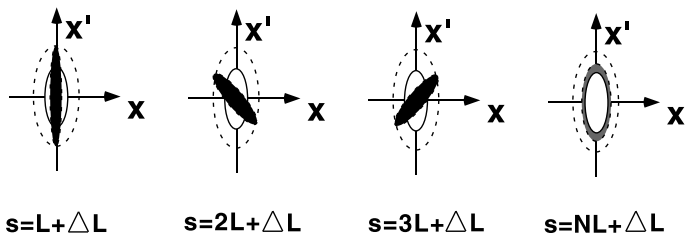

Fig. 4.9. Schematic of the horizontal phase space for a mismatched beam in a periodic linear lattice after 1, 2, 3 and $N \gg 1$ periods. The emittance is not preserved: the dilution is given by the ratio of the areas of the hatched ellipse to the design ellipse (for $N \to \infty$)

b) Circular Lattice

For a circular accelerator, the periodicity is usually taken to be not the superperiodicity of the machine (i.e., the number of identical lattice sections), but the revolution period. The index n therefore represents the turn number. The mismatch B_{mag} most often arises from improper orientation of the beam ellipse at injection. Neglecting the constant phase offset $\chi_{\langle x^2 \rangle_0}$ in (4.57), the

equilibrium emittance is

$$\epsilon_n = \frac{\langle x^2 \rangle_n}{\beta} = \epsilon_0 \left[\mathrm{B_{mag}} + \sqrt{\mathrm{B_{mag}}^2 - 1} \cos(4\pi\nu) \right] , \tag{4.63}$$

where ν is the phase advance per turn. Shown in Fig. 4.10 is the evolution of the transverse phase space for $\mathrm{B_{mag}}$ along with the projections onto the horizontal axis. With a turn-by-turn beam size monitor, the mismatch can be measured directly by detecting the beam size changes at every turn. An example is given in Sect. 9.6.

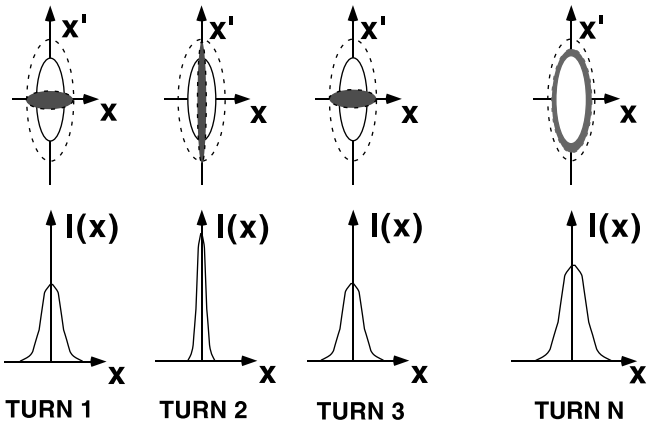

Fig. 4.10. Horizontal phase space and x-projection for a mismatched beam in a circular accelerator

4.2 Beta Matching in a Transport Line or Linac

The beam size (squared) at the location s can be expressed in terms of the α and β functions and the emittance at an upstream location s_0 as

$$\langle x^2(s) \rangle = R_{11}^2 \beta(s_0)\epsilon - 2R_{12}R_{11}\alpha(s_0)\epsilon + R_{12}^2 \gamma(s_0)\epsilon \, . \tag{4.64}$$

In a quadrupole scan, the transfer matrix elements R_{11} and R_{12} are varied, by changing the strength of a quadrupole between s_0 and s. Beam-size measurements for at least 3 different quadrupole settings are required in order to solve for the three independent unknown parameters: ϵ, $\beta(s_0)$ and $\alpha(s_0)$. The fourth parameter, $\gamma(s_0)$ is not free, but determined by $\alpha(s_0)$ and $\beta(s_0)$: $\gamma = (1 + \alpha^2)/\beta$.

The deviation of the β, α, and γ from the design parameters β_D, α_D and γ_D is often characterized in terms of the '$\mathrm{B_{mag}}$' (β matching) parameter [9, 10] of (4.59), which can also be written as

$$\mathrm{B_{mag}} = \frac{1}{2}\ \left(\beta\gamma_D - 2\alpha\alpha_D + \gamma\beta_D\right)\ . \tag{4.65}$$

Once the values of β and α are known, quadrupole magnets can be adjusted so as to match the optical functions at a selected point to their design value, which is equivalent to $\mathrm{B_{mag}} = 1$.

The SLC had more than 10 multi-wire emittance measurement stations, which monitored the beam emittances in various parts of the machine in hourly intervals, and were indispensable for emittance control and tuning. As will be shown in Sect. 4.4.3, in the SLC linac transverse orbit bumps were intentionally induced as a global correction which cancelled the accumulated local effects of dispersion or wakefields. The bumps were optimized by minimizing the emittance downstream, as calculated by this measurement technique.

Example. To illustrate the beta matching method, Fig. 4.11 shows an example from the KEK/ATF beam transport line (BT), connecting the S-band linac and the ATF damping ring. The top picture shows the result of a typical quadrupole scan at the end of the BT. Plotted is the square of the vertical beam size versus the strength of an upstream quadrupole, as well as a quadratic fit to the data. The Twiss parameters deduced from such a fit can be propagated through the BT, using a model derived from the actual or the design magnet settings. The bottom picture displays the inferred beta functions compared to the design optics.

4.3 Equilibrium Emittance

We now discuss different methods for changing and controlling the equilibrium emittance in electron or positron storage rings. In these rings, synchrotron radiation gives rise to an equilibrium beam size, which is independent of the beam emittance at injection. While at high beam currents, collective effects and intrabeam scattering may be important as well, at low beam intensity the value of the equilibrium emittance is determined solely by the ring optics and the beam energy.

The discreteness and the random character of the synchrotron radiation increases the beam emittance. The expression for the transverse emittance growth in the plane u ($u = x$ or y) due to quantum excitation is [12]:

$$\frac{\mathrm{d}\epsilon_u}{\mathrm{d}t} = cC_Q E^5 \left\langle \frac{\mathcal{H}_u}{\rho^3} \right\rangle\ , \tag{4.66}$$

where the function $\mathcal{H}_u$, introduced by Sands [13], is

$$\mathcal{H}_u(s) = \frac{1}{\beta_u}\left\{D_u^2 + \left(\beta_u D_u' + \alpha_u D_u\right)^2\right\}\ , \tag{4.67}$$

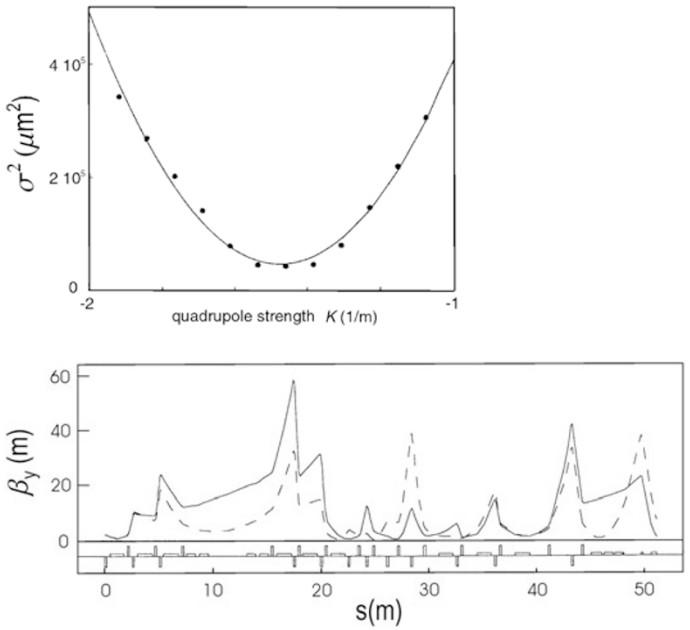

Fig. 4.11. Beta matching in the KEK/ATF beam transport line (BT) [11]: (*top*) quadrupole-scan emittance measurement; shown is the square of the vertical beam size measured using a fluorescent screen vs. the strength of an upstream quadrupole; (*bottom*) the vertical beta function obtained by propagating the measured Twiss parameters (*solid*) through the actual BT optics is compared with the beta function expected for the design optics (*dashed*)

the coefficient C_Q is

$$C_Q = \frac{55}{48\sqrt{3}} \frac{r_e \hbar c}{(m_e c^2)^6} \approx 2 \times 10^{-11}\ \mathrm{m}^2\ \mathrm{GeV}^{-5}\,. \tag{4.68}$$

and ρ is the bending radius. The angular brackets denote an average over the ring.

On the other hand, the average energy loss due to the synchrotron radiation usually leads to damping in all three degrees of freedom. The emittance decrease due to radiation damping is described by

$$\frac{\mathrm{d}\epsilon_u}{\mathrm{d}t} = -2\epsilon_u C_d J_u E^3 \left\langle \frac{1}{\rho^2} \right\rangle\,, \tag{4.69}$$

where ϵ is the beam emittance,

$$C_d = \frac{c}{3} \frac{r_e}{(m_e c^2)^3} = 2.1 \times 10^3\ \mathrm{m}^2\ \mathrm{GeV}^{-3}\ \mathrm{s}^{-1}\,, \tag{4.70}$$

and J_u is the damping partition number.

The equilibrium emittance is reached when the quantum excitation and the damping are equal. It is

$$\epsilon_{u,\infty} = C_q \frac{\gamma^2}{J_u} \frac{\left\langle \mathcal{H}_u / \rho^3 \right\rangle}{\langle 1/\rho^2 \rangle} \,, \tag{4.71}$$

where the new constant C_q is defined by

$$C_q = \frac{55}{32\sqrt{3}} \frac{\hbar c}{m_e c^2} = 3.84 \times 10^{-13} \text{ m} \,. \tag{4.72}$$

Thus ϵ_u is inversely proportional to the transverse damping partition number J_u. Similarly, the longitudinal emittance is inversely proportional to J_z.

The exponential amplitude-damping time τ_u is obtained from the equation

$$\frac{1}{\tau_u} \equiv \frac{1}{2\epsilon_u} \frac{\mathrm{d}\epsilon_u}{\mathrm{d}t} \,. \tag{4.73}$$

Including also the longitudinal degree of freedom, the exponential damping times for all three oscillation modes can be written as [13]

$$\tau_i = \frac{2E_0}{\langle P_\gamma \rangle J_i} \,, \tag{4.74}$$

where E_0 is the nominal energy, and $\langle P_\gamma \rangle$ is the average rate of energy loss. The latter is given by

$$\langle P_\gamma \rangle = \frac{c C_\gamma}{2\pi} E_0^4 \left\langle \frac{1}{\rho^2} \right\rangle \,, \tag{4.75}$$

where yet another constant is introduced, namely

$$C_\gamma = \frac{4\pi r_e}{3(m_e c^2)^3} \approx 8.877 \times 10^{-5} \text{ m GeV}^{-3} \,, \tag{4.76}$$

as defined by Sands [13].

The factor J_i in (4.74) is the damping partition number for the ith degree of freedom. A general theorem by Robinson [14] states that the sum of the three partition numbers is a constant:

$$J_x + J_y + J_z = 4 \,. \tag{4.77}$$

A general proof of this theorem is given in Chap. 11. If the ring only contains horizontal, but no vertical bending magnets, then $J_y = 1$ and the partition numbers in the other two planes are related by a term $\mathcal{D}$ [13]

$$J_x = 1 - \mathcal{D} \,, \tag{4.78}$$

$$J_z = 2 + \mathcal{D} \,, \tag{4.79}$$

where

$$\mathcal{D} = \frac{\oint D_x/\rho \ \left(1/\rho^2 + 2k\right) \, \mathrm{d}s}{\oint 1/\rho^2 \ \mathrm{d}s} \, . \tag{4.80}$$

For separated function magnets $k/\rho = 0$ and the value of $\mathcal{D}$ is typically much smaller than 1.

It is often desirable to increase one of the damping rates or to vary the horizontal emittance. For example, in linear collider applications, a fast horizontal damping and a small horizontal emittance are advantageous, whereas the longitudinal emittance is of less concern. In storage-ring colliders one may instead want to increase the horizontal emittance near the beam-beam limit[3].

The damping rate and the equilibrium emittance can be changed by adjusting the value of $\mathcal{D}$ and/or by adding wiggler magnets. Depending on the application, there are various possibilities to do so. In the following, we describe the effect of a change in the ring circumference, an almost equivalent application in which the accelerating frequency is changed, and two different applications of wigglers.

4.3.1 Circumference Change

If the geometric circumference of the ring is changed by moving the magnet centers outwards by a step Δx^{mag} while holding the ring rf frequency fixed (so as to maintain synchronization with other systems) the quantity $\mathcal{D}$ changes by

$$\Delta\mathcal{D} \approx -\left(\sum_q k_q^2 D_{x,q} L_q\right) \ \frac{2\rho^2}{C} \ \Delta x^{\mathrm{mag}} \, , \tag{4.82}$$

where k_q is the non-integrated quadrupole gradient, L_q the quadrupole length, $D_{x,q}$ the dispersion function at the quadrupole, C the ring circumference, and ρ the bending radius of the dipole magnets. The minus sign arises because the orbit moves inwards with respect to the quadrupole magnets (the orbit shift is opposite to the displacement: $\Delta x = -\Delta x^{\mathrm{mag}}$). Note that the contributions from focusing and defocusing magnets add, because the effect is quadratic in $k_{1,q}$. Note that $-2 < \Delta\mathcal{D} < 1$ else beam loss may occur at

[3] Near the beam-beam limit, experimental observations [15] have shown that attempts to raise the luminosity by increasing the bunch charge leads to an increase in the beam size such that the beam-beam tune shift, from (2.101),

$$\xi_x = \xi_y = \frac{r_e}{2\pi\gamma} \frac{N_b}{\epsilon_x(1+\kappa)} \tag{4.81}$$

(with $\kappa = \epsilon_y/\epsilon_x$ the emittance ratio), remains approximately constant. However, since $L \propto {N_b}^2/\epsilon$, such an increase in bunch charge and emittance still can result in a higher luminosity

the damping poles. The maximum tolerable shift Δx is determined by the available aperture, and by the beam size at injection.

In 1992, the magnet support girders of the SLC North Damping Ring were pulled outwards by about $\Delta x^{\mathrm{mag}} = 1.5$ mm, increasing the geometric ring circumference by 9 mm. As a result the measured horizontal damping time decreased [16] from 4.11 ± 0.11 ms to 3.41 ± 0.09 ms, consistent with predictions.

4.3.2 RF Frequency Change

An equivalent change in $\mathcal{D}$ can be achieved with a shift of the rf frequency by

$$\frac{\Delta f_{\mathrm{rf}}}{f_{\mathrm{rf}}} = \frac{2\pi \Delta x^{\mathrm{mag}}}{C} \,. \tag{4.83}$$

More accurately, the orbit shift in the quadrupole is proportional to the local dispersion function

$$\Delta x(s) = -\frac{D_x}{\alpha_x} \, \frac{\Delta f_{\mathrm{rf}}}{f_{\mathrm{rf}}} \,, \tag{4.84}$$

with α_c the momentum compaction factor. The change in the partition number is

$$\Delta \mathcal{D} \approx \frac{\oint 2k^2 D_x^2 \, \mathrm{d}s}{\oint \mathrm{d}s/\rho^2} \, \frac{\Delta p}{p} \equiv C_0 \, \frac{\Delta p}{p} \,. \tag{4.85}$$

However, in practice the rf frequency must be locked to the rf of the injection (or extraction) system. Therefore, at the SLC damping rings in addition to the static circumference change a dynamic rf frequency shift was implemented [17]. The dynamic rf frequency shift by up to 100 kHz started about 1.33 ms after injection, and was stopped 200 μs before extraction, in order to stabilize the injected beam and to minimize emittance and extraction jitter, respectively [18]. The total store time was 8.33 ms, equal to about 2.5 nominal damping times. For a dynamic frequency shift of 62.5 kHz the normalized emittance of the extracted beam decreased from 3.30 ± 0.07 m to 2.66 ± 0.06 m. The 20% reduction agreed with SAD calculations [17]. This example is discussed further in Sect. 8.10 after describing the influence of heavy beam loading on the rf system.

Emittance control via the accelerating rf has been used already before [19]. More recently it was applied at LEP [20] and in the HERA electron ring [21]. At HERA the associated increase in beam energy spread was compensated by a larger rf bucket height. With limited rf power, this was achieved by increasing the transverse focussing thereby reducing the dispersion and hence the momentum compaction factor.

We note an interesting side effect, remarked by Wiedemann [12]. From (4.85) the partition number changes with the particle momentum. If a particle performs synchrotron oscillations

$$\frac{\Delta p}{p} = \delta_{\max} \sin \Omega_s t \,, \tag{4.86}$$

its horizontal partition number and damping time vary with the synchrotron period:

$$\frac{1}{\tau} = \frac{1}{\tau_0}(1 - C_0 \delta_{\max} \sin \Omega_s t) \,, \tag{4.87}$$

The equation for the horizontal equilibrium emittance of such particles is then time-dependent according to [12]

$$\epsilon_x(t) = \epsilon_{x,\infty} \ \exp\left[\frac{2\delta_{\max} C_0}{\Omega \tau_0}(\cos \Omega t - 1)\right] . \tag{4.88}$$

The effect is largest for particles with large synchrotron oscillations.

4.3.3 Wigglers

A wiggler magnet generates additional synchrotron radiation and, thus, can enhance the radiation damping and/or change the equilibrium emittance. The damping time is modified as

$$\tau_{u,w} = \tau_{u,0} \frac{1}{1 + \langle 1/\rho^2 \rangle_w / \langle 1/\rho^2 \rangle_0} \,, \tag{4.89}$$

where $\tau_{u,x}$ is the damping time in the plane u including the effect of the wiggler, $\tau_{u,0}$ on the right is the damping time for the ring proper, while on the right-hand side of the equality, the subindex 0 indicates an average over the ring without wiggler magnets, while the subindex w indicates the contribution from the wiggler magnets. On the left, $\tau_{u,x}$ is the damping time in the plane u, including the effect of the wiggler, and $\tau_{u,0}$ on the right is the damping time for the ring proper.

Similarily, the relative emittance increase due to the presence of the wiggler is

$$\frac{\epsilon_{u,w}}{\epsilon_{u,0}} = \frac{1 + \left\langle \mathcal{H}_u/\rho^3 \right\rangle_w / \langle \mathcal{H}_u/\rho^3 \rangle_0}{1 + \langle 1/\rho^2 \rangle_w / \langle 1/\rho^2 \rangle_0} \,, \tag{4.90}$$

where the averages are given, for example, by

$$\left\langle \frac{1}{\rho^2} \right\rangle_w = \frac{1}{C} \oint \frac{1}{\rho_w^2} \, \mathrm{d}s \,, \tag{4.91}$$

with C the circumference, and ρ_w the bending radius in the wiggler.

In addition to changing the emittance, wigglers also affect the energy spread [12]:

$$\frac{\sigma_{\delta,w}^2}{\sigma_{\delta,0}^2} = \frac{1 + \left\langle 1/\rho^3 \right\rangle_w / \langle 1/\rho^3 \rangle_0}{1 + \langle 1/\rho^2 \rangle_w / \langle 1/\rho^2 \rangle_0} \,. \tag{4.92}$$

Damping Wigglers. If we place a wiggler in a region with no dispersion, $D_x = 0$, we might expect that the equilibrium emittance decreases according to (4.90) with $\langle H_w \rangle = 0$. However this is not completely correct, because the wiggler itself generates dispersion. As an example, we consider a sinusoidal wiggler with field

$$B(z) = B_w \cos k_p z \,, \tag{4.93}$$

where $k_p = 2\pi/\lambda_p$ and λ_p denotes the length of the wiggler period. The differential equation for the dispersion function reads:

$$D_u''(z) = \frac{1}{\rho_w} \cos k_p z \,, \tag{4.94}$$

which, assuming $D_u(0) = D_u'(0) = 0$, can be solved as

$$D_u(z) = \frac{1}{k_p^2 \rho_w} (1 - \cos k_p z) \,. \tag{4.95}$$

Using

$$\frac{1}{\rho} = \frac{1}{\rho_w} |\cos k_p z| \,, \tag{4.96}$$

for each half period of the wiggler we find [12]

$$\int_0^{\lambda_p/2} \frac{\mathcal{H}_u}{|\rho|^3} \, \mathrm{d}z = \frac{36}{15} \frac{1}{\beta_u} \frac{1}{k_p^5 \rho_w^5} + \frac{4}{15} \frac{\beta_u}{k_p^3 \rho_w^5} \approx \frac{4}{15} \, \frac{\beta_u}{k_p^3 \rho_w^5} \,, \tag{4.97}$$

where β is the beta function and we assumed that $\lambda_p \ll \beta$. Introducing the deflection angle per wiggler pole $\theta_w = 1/(\rho_w k_p)$, and the number of wiggler periods N_w, we can rewrite (4.97) as

$$\int_w \frac{\mathcal{H}_u}{\rho^3} \, \mathrm{d}z \approx N_w \frac{8}{15} \frac{\beta}{\rho_w^2} . \theta_w^3 \tag{4.98}$$

Similarily, we find

$$\int_w \frac{1}{\rho^2} \, \mathrm{d}z \approx \pi N_w \frac{\theta_w}{\rho_w} \,. \tag{4.99}$$

Finally the emittance ratio, (4.90), becomes

$$\frac{\epsilon_{u,w}}{\epsilon_{u,0}} = \frac{1 + \frac{8}{30\pi} N_w \frac{\beta_u}{\langle \mathcal{H}_u \rangle_0} \frac{\rho_0^2}{\rho_w^2} \theta_w^3}{1 + \frac{1}{2} N_w \frac{\rho_0}{\rho_w} \theta_w} \,, \tag{4.100}$$

where $\langle \mathcal{H}_u \rangle_0$ is the average value of $\mathcal{H}_u$ in the ring magnets, excluding the wiggler magnets. The latter can be re-expressed in terms of the emittance ϵ_{x0} to yield, e.g., with a vertical wiggler field, the horizontal emittance

$$\frac{\epsilon_{x,w}}{\epsilon_{x,0}} = \frac{1 + \frac{8C_q}{30\pi J_x} N_w \frac{\beta_x}{\epsilon_{x0} \rho_w} \gamma^2 \frac{\rho_0}{\rho_w} \theta_w^3}{1 + \frac{1}{2} N_w \frac{\rho_0}{\rho_w} \theta_w} \,. \tag{4.101}$$

The emittance is reduced by the wiggler magnet if

$$\frac{8}{15\pi}\frac{C_q}{J_x}\frac{\beta_x}{\epsilon_0\rho_w}\,\gamma^2\theta_w^2 \le 1\,. \tag{4.102}$$

In a wiggler-dominated ring the minimum emittance which one might hope to achieve is still limited. Ignoring the contributions from the arcs, after traversing a large number of wiggler periods (with intermittent re-acceleration) the emittance reaches an asymptotic value

$$\epsilon_{x,w} \to \frac{16}{30\pi}\frac{C_q\beta_x}{\rho_w}\gamma^2\theta_w^2\,. \tag{4.103}$$

The horizontal damping time with a wiggler can be written as

$$\tau_{x,w} = \tau_{x,0}\frac{1}{1+\frac{1}{2}N_w\frac{\rho_0}{\rho_w}\theta_w}\,. \tag{4.104}$$

In the limit of an extremely wiggler-dominated ring or a very long wiggler channel, again assuming intermittent re-acceleration, this simplifies to

$$\tau_{x,w} \approx \frac{2\rho_w^2}{C_d J_x E^3}\,. \tag{4.105}$$

Equations (4.103) and (4.105) set lower bounds on the emittance and damping times that can be attained in the damping ring of a future linear collider.

Robinson wiggler. A "Robinson wiggler" is a wiggler consisting of a series of combined function magnets, arranged such as to increase the horizontal partition number. Such a magnet was first used at the CEA to convert the synchrotron (which because $\mathcal{D} > 1$ was horizontally unstable) into a stable storage ring with $0 < \mathcal{D} < 1$ [14]. Such a wiggler will change the partition number according to [22]

$$\Delta\mathcal{D} \approx \frac{\bar{D}_x L_{\mathrm{Rob}} k}{2\pi(1+F_\omega)}\frac{\rho_0}{\rho_{\mathrm{Rob}}}\,, \tag{4.106}$$

where L_{Rob} and ρ_{Rob} are the length and the bending radius of the Robinson wiggler, $\bar{D}_x$ the average dispersion in the wiggler, ρ_0 the bending radius of the main bends, k the magnitude of the wiggler quadrupole gradient (in units of m^{-2}), and

$$F_\omega \equiv \frac{1}{2}N_w\frac{\rho_0}{\rho_w}\theta_w\,. \tag{4.107}$$

Unfortunately, the Robinson wiggler not only increases the damping but it can also blow up the equilibrium emittance, since it is preferably placed at a location with large dispersion.

Other wigglers. Further applications of wigglers include polarization wigglers for electron storage rings. These decrease the polarization time at low beam energies [23] or invert the spin direction [24].

4.4 Linac Emittance Control

4.4.1 Introduction

Preservation of the beam emittances in a linear accelerator differs from that in a lepton storage ring since in a linac there is no or little radiation damping. The normalized beam emittance therefore may increase due to many different effects.

In an electron linac, emittance dilutions may occur due to alignment errors of the accelerator components, which arise from steering the beam through misaligned structures and quadrupole magnets using beam-position monitors with residual offset errors [29]. The resulting transverse wake fields and dispersive effects increase the beam emittance. Some countermeasures that have been developed to minimize linac emittance growth are BNS damping, trajectory oscillations or 'wake field bumps', and dispersion-free steering, which we have already encountered in the previous chapter. In this section we discuss the BNS damping in more detail. We also present a further example for the application of 'wake field bumps' in the SLC, and briefly recall the underlying concept of dispersion-free steering.

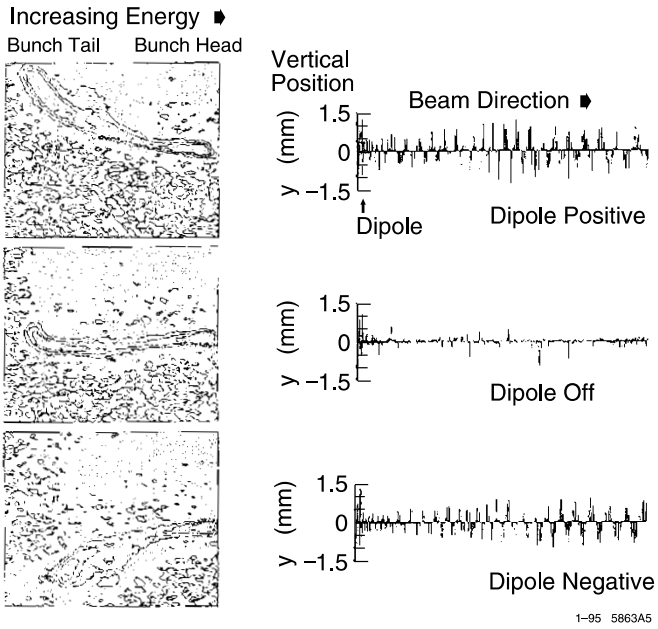

Fig. 4.12. Profile monitor measurements in a region of nonzero dispersion after the end of the SLC linac and vertical centroid trajectories with a positive purturbation to the bunch orbit (*top*), under nominal conditions (*middle*), and with a negative perturbation (*bottom*) (Courtesy J. Seeman, 2000)

As an example, Fig. 4.12 shows profile monitor measurements and trajectories for three different initial vertical displacements [25] of the linac beam in the SLC. The middle plots correspond to an optimized orbit. In the top plots the beam was kicked in one direction and in the bottom plot in the other direction. The increase in vertical amplitude towards the tail of the bunch shows the intrabunch particle displacements due to the transverse wakefields. Also evident from this measurement is a position-energy correlation[4]. The observed decrease in energy along the bunch depends on the cancellation between the rf slope due to the induced field and the rf slope of the accelerating rf (see Chap. 8).

Viewed independently, shown in Fig. 4.13 are the transverse beam profiles measured at the end of the linac for various initial beam displacements [26]. These measurements were made [27] by deflecting the beam using a fast kicker magnets located within the linac so that the true transverse profile $y(x)$ is represented. Notice that while the slice emittances of Fig. 4.12 are almost constant, the projected emittance is significantly increased as shown in Fig. 4.13.

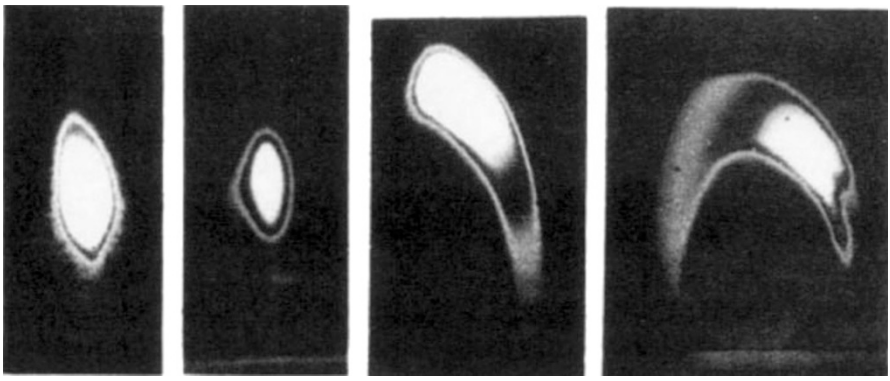

Fig. 4.13. Measured beam profiles demonstrating emittance growth due to wakefields as a function of increasing oscillation amplitude. From *left* to *right* the amplitudes in the applied horizontal trajectory displacement are 0 mm, 0.2 mm, 0.5 mm, and 1.0 mm. The single-bunch charge was 2×10^{10} electrons (Courtesy J. Seemann, 2000)

4.4.2 BNS Damping

The wake field effect can be reduced by proper adjustment of the rf phase profile along the linac. By passing the rf wave off-crest a position-energy

[4] these measurements were obtained by deflecting the beam onto a fluorescent screen using a kicker magnet located in a dispersive region (in the collider arcs) so that the measured horizontal position indicates an energy deviation; i.e., the profile monitor shows $y(E)$

correlation is generated along each linac bunch, such that the tail particles have lower energy than the particles in the bunch head. This results in so-called BNS damping [28], where the defocusing due to the wake fields is compensated by the stronger focusing for lower-energy tail particles.

To illustrate the mechanism, consider a 2-particle model, each with half the total bunch charge and a distance z apart. Let the first (head) particle be at the design energy and assume that the bunch head performs a pure betatron oscillation,

$$y_1(s) = \hat{y} \cos s/\beta \,, \tag{4.108}$$

with β the average vertical beta function. For simplicity. we here employ a smooth approximation for the betatron oscillation and the lattice focusing, i.e., the beta function is constant. Then the equation of motion for the second particle with a relative momentum deviation $\delta \equiv \Delta p/p_0$ (p_0 denotes the design momentum) is [30]

$$\frac{\mathrm{d}y_2(s)}{\mathrm{d}s^2} + \frac{1}{\beta^2(\delta)} y_2(s) = \frac{N r_e W_1(z)}{2\gamma L} \hat{y} \cos s/\beta \,, \tag{4.109}$$

where $W_1(z)$ denotes the value of the transverse wake function per cavity (in units of m^{-2}), N is the bunch population, and L the cavity period. We have ignored the effect of acceleration.

Equation (4.109) shows that there exists a value of δ for which, in first order, the bunch tail exactly follows the bunch head. Writing $\beta(\delta) = \beta(0) + \Delta\beta(\delta)$ this value corresponds to [30]

$$\frac{\Delta\beta(\delta)}{\beta(0)} = -\frac{N_b r_e \beta^2 W_1(z)}{4\gamma L} \,, \tag{4.110}$$

a condition which is also known as 'autophasing'. The relative change in beta function as a function of energy can easily be expressed using the linac chromaticity ξ using the relation

$$\frac{\Delta\beta}{\beta} = -\xi\delta \,. \tag{4.111}$$

For an optical FODO cell, we have

$$\xi = -\frac{2}{\mu} \tan\frac{\mu}{2} \,, \tag{4.112}$$

where μ is the betatron phase advance per cell. In case of an accelerated beam, the autophasing condition is still given by (4.110), if we simply replace the factor $1/\gamma$ by $\ln(\gamma_f/\gamma_i)/\gamma_f$ where γ_i and γ_f characterize the initial and final energies in units of the rest mass.

In practice, BNS damping can only partially be realized, since the energy spread introduced at low energies must be restored later in the linac to fit inside the energy acceptance of the downstream beam delivery system.

4.4.3 Trajectory Oscillations

In addition to BNS damping, empirically distributing a set of short-range oscillations, or wake-field bumps (see Sect. 3.6), along the accelerator proved indispensable for SLC operation [29]. Examples of betatron oscillations intentionally induced in the SLAC linac are shown in Fig. 4.14 [29].

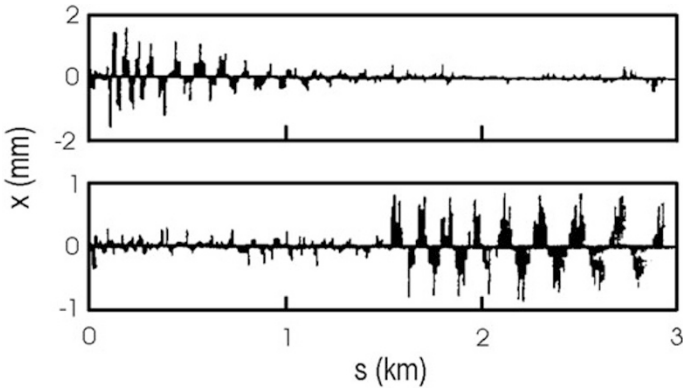

Fig. 4.14. Two trajectory ocillations in the SLAC linac, which were used to study the effect on the downstream emittance (Courtesy F.J. Decker, 1999)

Wakefields and dispersive effects in the linac generate both emittance growth and a mismatch. The mismatch induced early in the linac has completely filamented when the beam reaches its end, while perturbations near the linac end also result in residual unfilamented tails and in a phase-space mismatch, which is conventionally characterized by the parameter B_{mag}, (4.59). This factor specifies the emittance growth after filamentation. A matched beam fulfills $B_{mag} = 1$.

Similarily, trajectory oscillations induced in the early parts of the linac only change the beam emittance $\gamma\epsilon$, while those in the latter sections also affect the measured betatron mismatch. This is illustrated in Fig. 4.15, which displays the measured normalized emittance versus the amplitude of the two trajectory bumps in Fig. 4.14.

The SLC employed a series of more than 10 orbit feedback loops with roughly equidistant spacing along the SLAC linac. These feedbacks continually maintained constant values of offset and slope at certain pairs of beam-position monitors, by adjusting the strengths of a few steering correctors. The feedback set points for position and slope were set to empirically determined target values.

A closed trajectory oscillation was most easily generated by changing a feedback set point (for either slope or position). The induced trajectory oscillation was then automatically taken out by the next feedback downstream, because the latter attempted to restore the original orbit.

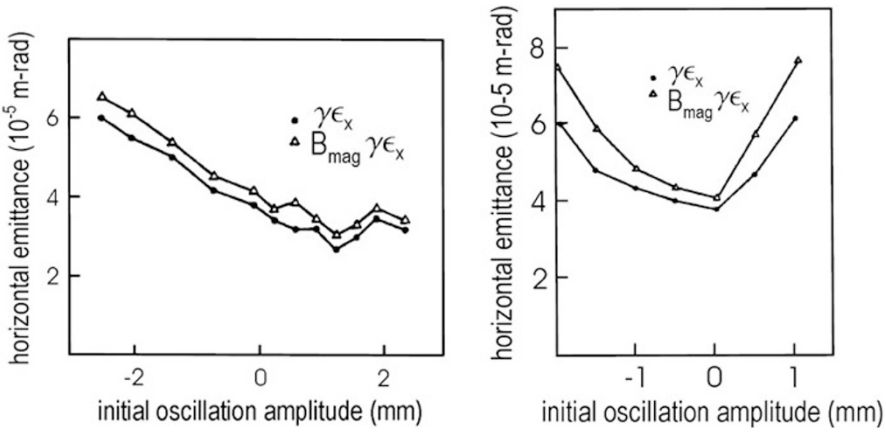

Fig. 4.15. Change in the normalized emittance as a function of the amplitude of a trajectory oscillation induced early in the linac (*left*) and towards the end of the linac (*right*). In the first case, the betatron mismatch is constant, and the normalized emittance decreased by 25% for an oscillation amplitude of about 1.5 mm. In the lower plot, the trajectory oscillation applied later in the linac did not reduce the normalized emittance. Instead it enhances the observed betatron mismatch, which is evident by the separation of the two curves representing $\gamma\epsilon$ and $B_{mag}\gamma\epsilon$ (Courtesy F.J. Decker, 1999)

In the later years of SLC operation, typical oscillation amplitudes were of the order of 100 or 200 μm, comparable to the presumed misalignments of the accelerating structures.

4.4.4 Dispersion-Free Steering

A very efficient steering algorithm has been developed in order to minimize the dispersive emittance growth in a linac. By its effect, this method is known as 'dispersion-free steering' [31, 32]. The detailed algorithm was already presented in Sect. 3.7, in the context of orbit correction schemes.

The basic idea of this method is to steer the orbit such that the particle trajectories become independent of the particle energy. In practice this can be achieved, for example, by exciting the steering coils (orbit correctors), so as to minimize the orbit response to a constant relative change of all quadrupole strengths.

During initial studies of this algorithm, the quadrupoles and correctors were so scaled to mimic the change in beam energy. In later years, instead, advantage was taken of the fact that both electron and positron bunches traversed the same linac. As far as dispersion is concerned, a change in the sign of the charge is equivalent to a 200% energy variation.

The so-called two-beam dispersion-free steering then consisted in measuring the orbit of both electron and positron beams, and correcting the

absolute orbit offset of one beam as well the difference to the orbit of the other beam. At the same time, the overall excitation strength of the steering correctors was also constrained. This steering method was implemented in the SLC control system by means of an SVD algorithm (SVD or *singular value decomposition* was discussed in Sect. 3.5), where weighting factors could be assigned to the different minimization constraints. Two-beam dispersion-free steering was also applied with great success at the circular collider LEP [33].

Exercises

4.1 Beta Mismatch

Suppose a beam is injected with a distribution characterized by optical functions β, α and γ different from the matched values β_0, α_0 and γ_0. Show that the beam emittance after filamentation is given by $\epsilon = \mathrm{B_{mag}}\ \epsilon_0$, where ϵ_0 is the initial emittance of the injected beam, and $\mathrm{B_{mag}}$ was defined in (4.65). Hint: filamentation corresponds to a randomization of the betatron phase and $\epsilon = \langle I \rangle$.

4.2 Propagation of Twiss Parameters

In Fig. 4.11 the Twiss parameters were measured at a single location yet the 'measured' values were shown as a function of position along the transport line. Derive the matrix for propagation of the Twiss parameters from a known location to an arbitrary location along the transport line. Hint: use the equation for a general phase space ellipse of area ϵ (not to be confused with the rms emittance)

$$\gamma x^2 + 2\alpha x x' + \beta x'^2 = \epsilon\,, \tag{4.113}$$

the relation $\beta\gamma - \alpha^2 = 1$, and the 2×2 transport matrix of the form

$$\begin{pmatrix} x \\ x' \end{pmatrix} = \begin{pmatrix} C(s) & S(s) \\ C(s)' & S(s)' \end{pmatrix} \begin{pmatrix} x_0 \\ x_0{}' \end{pmatrix}\,. \tag{4.114}$$

4.3 Static and Dynamic change of Partition Numbers

Assume parameters typical for the SLC damping rings: 40 quadrupoles, $k_q \approx 15\ \mathrm{m}^{-2}$, $D_{x,q} \approx 0.15$ m, $L_q \approx 18$ cm, $\rho \approx 1/2\ C/(2\pi)$, $C = 35$ m, harmonic number $h = 84$, rf frequency $f_{\mathrm{rf}} = 714$ MHz, and momentum compaction $\alpha = 0.0147$.

a) What is the change in $\mathcal{D}$ for an outward shift of all magnets by $\Delta x = 1.5\,\mathrm{mm}$?

b) What would be the equivalent change in the rf frequency?

4.4 Effect of Wiggler on Equilibrium Emittance

Consider a ring which consists mainly of wiggler magnets, with a peak magnetic field B_w of 40 kG, and a wiggler oscillation period of λ_p of 20 cm. Calculate the equilibrium emittance and the damping time in such a ring, assuming a beta function β_x of 5 m, and beam energies of 1 GeV and 5 GeV. Compare this with a typical damping-ring design for a future linear collider, where $\gamma\epsilon_x \approx 3$ μm, and $\tau_x \approx 3$ ms.

4.5 BNS Damping at the SLC

For the SLAC linac $\beta \approx 20$ m, $W_\perp(1 \text{ mm}) \approx 1 \text{ cm}^{-2}$, $L = 3.5$ cm, $N = 4 \times 10^{10}$, $\mu \approx \pi/2$, with an injected beam energy of 1.2 GeV and a final energy of 47 GeV. How large is the BNS energy chirp δ over the bunch length of 1 mm?